Scanning-Free Solid-State Biased THz Waveform Detection from 1 to 30 THz

Ohrt, Alexander H.; Zhou, Siyan; Cheng, Long; Rasmussen, Mattias; Ding, Yunhong; Jepsen, Peter U.; Zhou, Binbin

Published in:
Ultrafast Science

Link to article, DOI:
10.34133/ultrafastscience.0089

Publication date:
2025

Document Version
Publisher's PDF, also known as Version of record

Ultrafast Science
A SCIENCE PARTNER JOURNAL

RESEARCH ARTICLE

Scanning-Free Solid-State Biased THz Waveform Detection from 1 to 30 THz

Alexander H. Ohrt*, Siyan Zhou, Long Cheng, Mattias Rasmussen, Yunhong Ding, Peter U. Jepsen, and Binbin Zhou*

Department of Electrical and Photonics Engineering, Technical University of Denmark, 2800 Kgs. Lyngby, Denmark.

*Address correspondence to: ahooh@dtu.dk (A.H.O.); zhou@dtu.dk (B.Z.)

Citation: Ohrt AH, Zhou S, Cheng L, Rasmussen M, Ding Y, Jepsen PU, Zhou B. Scanning-Free Solid-State Biased THz Waveform Detection from 1 to 30 THz. *Ultrafast Sci.* 2025;5:Article 0089. https://doi.org/10.34133/ultrafastscience.0089

Submitted 21 October 2024
Revised 11 February 2025
Accepted 16 February 2025
Published 6 March 2025

Recent advancements in high-energy terahertz (THz) sources, driven by powerful laser systems, now enable the generation of ultrashort THz pulses with energies up to several millijoules, spanning frequencies from 1 to 30 THz. A key breakthrough is developing a reliable single-shot detection method, essential for measuring the electric field of these broadband, low-repetition-rate pulses, which is vital for exploring the complex dynamics of THz emission and studying extreme nonlinear material responses in this range. Existing detection methods have been limited to lower frequencies. Here, we introduce the first potentially single-shot-capable THz detection technique for capturing ultra-broadband waveforms. Utilizing a 1-μm-thick SiN detection chip, we exploit THz field-induced second harmonic generation to achieve real-time monitoring of THz waveforms with frequency content up to 30 THz. By adjusting the angle between the THz and optical probe beams, we can fine-tune the detection window for enhanced flexibility. Our novel THz detector is ideally suited for high-energy, low-repetition-rate sources, unlocking new frontiers in THz research.

Introduction

The terahertz (THz) region of the electromagnetic spectrum offers a wealth of physical, chemical, and biological light–matter interactions. THz time-domain spectroscopy (THz-TDS) offers essential insights into material properties by exploring these interactions and has emerged as a transformative tool across various scientific disciplines [1]. Standard THz-TDS measures the time-dependent waveform of the THz electric field through sequential time delay scans between the THz and an optical probe pulse, recording each point individually. Although this method provides excellent detection sensitivity and signal-to-noise ratio (SNR), it has notable drawbacks. It is time-intensive, especially problematic for multi-dimensional THz spectroscopy, and unsuitable for observing nonrepetitive or irreversible processes with characteristic time constants faster than the total sampling time of the waveform, such as structural phase transitions or material degradation. Standard THz waveform detection techniques particularly struggle with low-repetition-rate signals that exhibit substantial shot-to-shot variations.

Single-shot THz detection methods represent a paradigm shift by enabling parallel, scanning-free waveform acquisition, overcoming the limitations of traditional scanning systems. These techniques have been intensively explored, either by spatial–temporal coupling, which encodes temporal delay information onto the spatial extent of the probe beam via noncollinear geometry or collinear tilted pulse front, or by spectral–temporal coupling where temporal information is encoded onto the spectral domain via a linearly chirped optical probe pulse [2]. Most reported THz single-shot detection techniques employ the electro-optic (EO) sampling technique due to its high sensitivity and ease of implementation. However, phonon absorption and phase-matching condition issues in EO sampling crystals limit the demonstrated bandwidth to only a few THz, regardless of the bandwidth of THz emission sources [2,3]. Recent progress has been mostly in achieving ultra-high THz waveform acquisition speed [4] but rarely in improving the detection bandwidth. There is an urgent need for single-shot THz detection with broader bandwidth. Large-scale laser facilities have recently reported THz pulse generation up to multiple millijoule levels from both gaseous and solid targets [5–7]. These inherently single-shot THz pulses are intrinsically broadband with bandwidths exceeding 30 THz. However, current single-shot THz waveform detection can only measure electrical field components at the low-frequency end. Therefore, major parts of THz frequencies are only accessible via single-shot autocorrelation [8], interferometry [9], or THz power measurements combined with various bandpass filters [5–7], none of which offer coherent detection that retains the phase information. When detected with high fidelity, the temporal THz waveform contains a direct imprint of the polarization dynamics of the underlying generation mechanism ($E_{\mathrm{THz}}(t) \propto \partial^2 P / \partial t^2$) [10], so direct THz waveform detection capable of capturing such ultra-broadband transient signals would provide key insights into the intricate THz emission mechanisms and open immense opportunities for exploring extreme nonlinear material responses across the THz regime.

In the mid-infrared (MIR) range, single-shot electrical field detection has been successfully reported using the tunneling

ionization with a perturbation (TIPTOE) technique [11,12] or by monitoring electron emission from large-area nanoantenna arrays [13]. However, these methods cannot be straightforwardly applied to the THz regime due to the significantly lower available peak electrical field at the focus spot, which is insufficient for driving the highly nonlinear tunnel ionization process. The 4-wave mixing (FWM)-based nonlinear upconversion process in gas medium has been employed for ultra-broadband single-shot characterization in MIR spectrum detection [14,15] and detecting the electrical field of sub-single-cycle infrared pulses across MIR down to approximately 10 THz [16]. Despite the system's complexity, the reported detection sensitivity at frequencies below 10 THz is rather weak.

The first practical single-shot waveform detection technique to cover the entire THz frequency range remains an open challenge. Recently, Francis and colleagues [17,18] presented a scheme relying on FWM upconversion, or THz field-induced second harmonic (TFISH) generation locally within an air plasma, where the THz field intensity is orders of magnitude stronger than at the far-field focus. This method demonstrated a detection bandwidth approaching 20 THz (up to 10 THz at −10 dB level). However, its application is limited since the single-shot detection must occur within the same air plasma used for THz generation.

Based on recent developments in solid-state biased coherent detection (SSBCD) [19,20] and the significantly enhanced sensitivity from thin-film media with third-order nonlinearities ($\chi^{(3)}$) compared to conventional gas media, this article presents the first scanning-free, potentially single-shot-capable, THz waveform detection technique that both is practically compatible with spectroscopy applications and spans the entire THz spectrum (up to 30 THz). It is particularly well-suited for high-energy THz pulses driven by large-scale laser facilities.

Materials and Methods

Design considerations

Single-shot waveform detection of ultra-broadband THz pulses has significantly different requirements from standard single-shot techniques for sub-picosecond THz transient detection. Standard techniques usually feature a time delay (temporal step size) of a few tens of femtoseconds (e.g., 50 fs) and a time window of about 10 ps. However, the fast-oscillating field of ultra-broadband THz pulses necessitates much finer time delay steps (a few femtoseconds) and a total measurement time window of a few picoseconds to capture the full waveform for THz-TDS applications. The spectral–temporal coupling single-shot technique usually involves a minimum time delay much larger than 10 fs, making it impractical for ultra-broadband THz detection. Recently, significant progress has been made in single-shot THz detection using the reflective-echelon-based EO sampling technique [3,21]. Encoding temporal delay with a reflective echelon presents a potentially viable solution for single-shot ultra-broadband THz waveform detection. However, achieving the fine temporal step size required for ultra-broadband waveform detection poses fabrication challenges for these delicate echelon devices. Even a successfully fabricated echelon surface tends to diffract a significant portion of the incident optical probe beam, causing unfavorable beam distortions. The poor reflection efficiency of the echelon surface also causes thermal and other adverse effects.

Here, we adopt a well-known single-shot technique that uses a noncollinear probe-THz geometry to convert a temporal probe-THz delay to pixels on a spatially resolved detector [22]. As will be illustrated in detail below, this noncollinear probe-THz geometry cannot support ultra-broadband detection under standard detection conditions. However, by combining the noncollinear probe-THz interaction with the high-sensitivity thin-film SSBCD technique, we achieve an ideal setting for detecting ultra-broadband THz transients.

In the noncollinear configuration, as shown in Fig. 1A, both THz and optical probe beams are focused to lines that overlap in the active detection material at a slight angle, θ. The depth of the active detection material, d, refers to the thickness of the region where TFISH generation occurs. For the standard ultra-broadband detection technique, air-biased coherent detection (ABCD), where dry nitrogen gas acts as the detection medium, the effective detection depth d is typically a few millimeters, determined by the overlapping Rayleigh ranges of the probe and THz beams [23]. For the SSBCD, d is limited to the

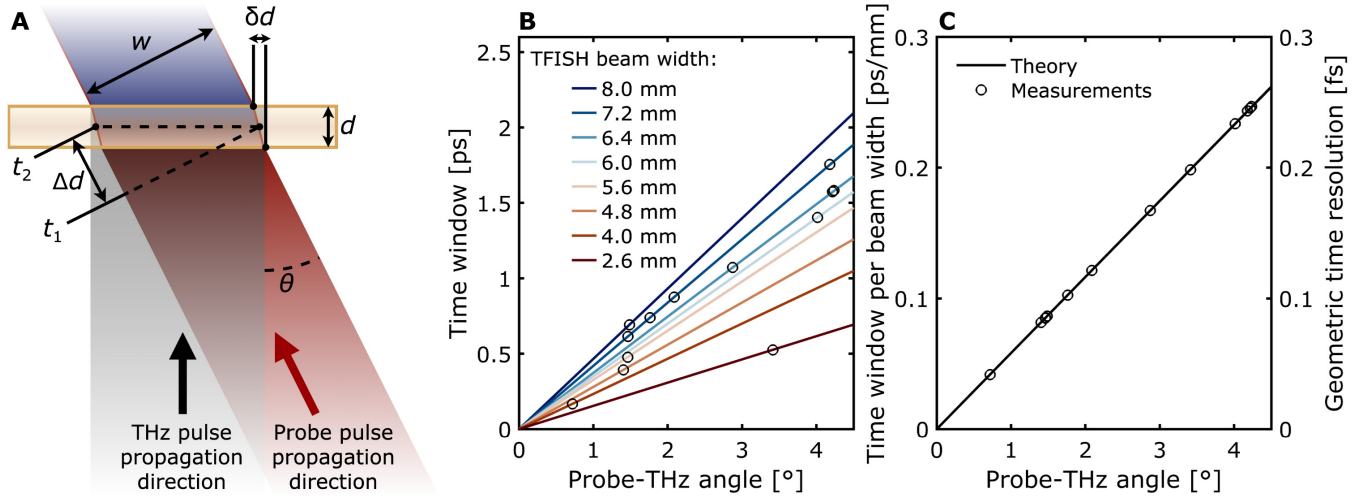

Fig. 1. (A) Top view schematic of the noncollinear probe-THz interaction. (B) Circles represent measurements of obtained time windows at different probe-THz angles and TFISH widths. The lines of various colors show the expected trends from Eq. 1 with TFISH widths obtained in measurements. (C) Time window normalized by TFISH width versus probe-THz angle. The circles are the same measurements as in (B), and the black line simply shows Eq. 1 normalized by w. The rightmost vertical axis is scaled to the expected time resolution limit versus probe-THz angle from Eq. 2.

thickness of the thin-film $\chi^{(3)}$ medium, which in our case is 1-μm-thick SiN [20]. Similarly, w denotes the effective width over which TFISH can be generated. This width is always smaller than the narrower of the probe or THz line focus widths. The effective time window attainable, Δt, is dependent on these parameters, including the probe-THz angle θ:

$$\Delta t = \frac{\Delta d}{c} = \frac{\tan(\theta) w}{c} \quad (1)$$

Δd is the probe-THz optical path length difference between the leftmost part and the rightmost part of the detection region in Fig. 1A where the probe and THz lines overlap. In experimental configurations (see Fig. 1B), Δd typically exceeds d by a factor of more than 100. The time-to-space encoding therefore occurs almost entirely during free-space propagation of the optical probe with its free-space probe-THz angle θ, even though this is not directly apparent in the schematic. In consequence, it is not necessary to consider the change in probe-THz angle inside the detection medium due to refraction when determining the time window size.

In Fig. 1B, Δt from Eq. 1 is plotted against θ for different w values based on measured TFISH widths. The circles on the lines in Fig. 1B represent experimentally obtained time windows at measured probe-THz angles and TFISH widths. The data acquisition process is explained in the Results section. The figure indicates that time windows exceeding 0.5 ps—sufficient to fully capture an air-plasma-based THz waveform—can be achieved with a modest θ of approximately 1.5° when w is at least 5.6 mm. Larger time windows can be achieved by increasing θ or w. By normalizing Δt by w, the data points in Fig. 1B collapse onto a single line, shown in Fig. 1C, which matches the predicted trend from Eq. 1.

In the time-to-space encoding scheme, a figure of merit for the time resolution limit imposed by the finite depth of the detection region d is determined by the distance δd, and corresponding time δt that the probe beam travels in the direction parallel to the THz beam wavefront. Unlike the time window (Eq. 1), this effect is confined entirely to the detection medium. It is, therefore, necessary to consider the probe-THz angle θ_i inside the detection medium with refractive index n:

$$\delta t = \frac{n\delta d}{c} = \frac{n\tan(\theta_i) d}{c} \approx \frac{n\tan(\theta/n) d}{c} \approx \frac{\tan(\theta) d}{c} \quad (2)$$

The rightmost approximation in Eq. 2 holds for small probe-THz angles. It reveals that the geometric time resolution δt in this case is independent of n, since the decrease in physical distance δd due to the smaller internal probe-THz angle is compensated for by the slower phase velocity inside the medium relative to free space. The same is true for the time window; even if the detection medium was very thick (i.e., if $\Delta d >> d$ is not satisfied), the expression in Eq. 1 still holds for small probe-THz angles.

In a standard ABCD system, assuming a typical $d = 2$ mm as in our THz air-photonics platform, and with $\theta = 1.5°$, it results in $\delta t = 0.17$ ps. This time resolution may be acceptable for relatively narrow-band, sub-picosecond THz transient detection, but it is inadequate for ultra-broadband detection since the main waveform is typically shorter than 0.17 ps. In contrast, the extremely thin effective interaction depth of the SSBCD device supports a much higher time resolution. The rightmost vertical axis of Fig. 1C shows the expected time resolution limit versus free space probe-THz angle with 1-μm-thick SiN as the detection medium. A geometrically limited resolution of less than 0.24 fs for probe-THz angles below 4° is predicted, making it fully compatible with ultra-broadband detection.

Notably, the 3 orders of magnitude thinner active detection depth of the SiN-based solid-state detector (SSD) provides significantly higher detection sensitivity than ABCD. This is because SiN has a much higher $\chi^{(3)}$ coefficient than nitrogen [20]. Additionally, the 1-μm thickness imposes minimal limitations on phase matching and detection bandwidth. The high detection sensitivity is crucial in our scanning-free ultra-broadband detector, as it ensures the efficient generation of a TFISH line with sufficient length from the overlapped optical probe and THz lines, even when pulse intensities are significantly compromised compared to a standard point-focus situation. This eliminates the need to rely on a locally confined THz field within the air plasma for enhanced TFISH generation in single-shot detection, as mentioned in [17,18].

Implementation

A schematic of the setup is shown in Fig. 2A. A 40-fs, 2-mJ Ti:sapphire laser amplifier with a 1-kHz repetition rate is employed to drive the system. The horizontally polarized laser output passes through a 90% transmissive beamsplitter (BS). The transmitted beam generates ultra-broadband THz radiation via a standard 2-color air-plasma process. After collimation with an off-axis parabolic mirror ($f = 4''$), a high-resistivity silicon (HR Si) plate is used to eliminate all residual laser beams. The collimated THz radiation is subsequently directed onto a custom-designed 90° off-axis linear parabolic reflector, referred to as a 1D-OAP in the schematic. This reflector is flat/linear along one dimension and parabolic along another. The parabola's focal length varies along the reflector's surface, forming a line focus at a 90° angle to the incoming collimated light wavefront, aligned parallel to the reflected wavefront. The focal length from the center of the reflector to the center of the line focus is 40 mm, and the resulting line focus is roughly 80 μm thin, full width at half maximum (FWHM).

A small portion of the laser beam is focused by a cylindrical lens (L2) into a 40-μm thin line focus (FWHM). To facilitate the overlap between the THz and optical probe line focuses, the 1D-OAP is cut in half, capturing half of the collimated THz beam to form the line focus while allowing the optical probe beam to pass slightly above its top edge. The 2 line focuses overlap with a small adjustable angle between the beam wavefronts. Additional details on the 1D-OAP and the overlapping line focuses, including a THz camera image of the THz line focus, are provided in the Supplementary Materials (see Fig. S2B).

An image of the SSD is shown in Fig. 2B. It consists of gold electrodes arranged to form a 25-mm-wide and 100-μm-narrow slit, all covered by a 1-μm-thin layer of SiN. The 1-μm-thin SiN within the slit acts as the effective detection medium. The SSD structure rests on a 0.5-mm-thick SiO_2 substrate glued onto a printed circuit board (PCB). A bias voltage can be applied across the SiN-filled slit via the PCB using gold wire bonding. The maximum applicable bias voltage has been tested, and breakdown typically occurs at approximately 800 to 1,000 V, corresponding to a field strength of 80 to 100 kV/cm. In comparison, an SSD device using a similar SiN film as active material achieved a breakdown field of 212 kV/cm, suggesting potential for further

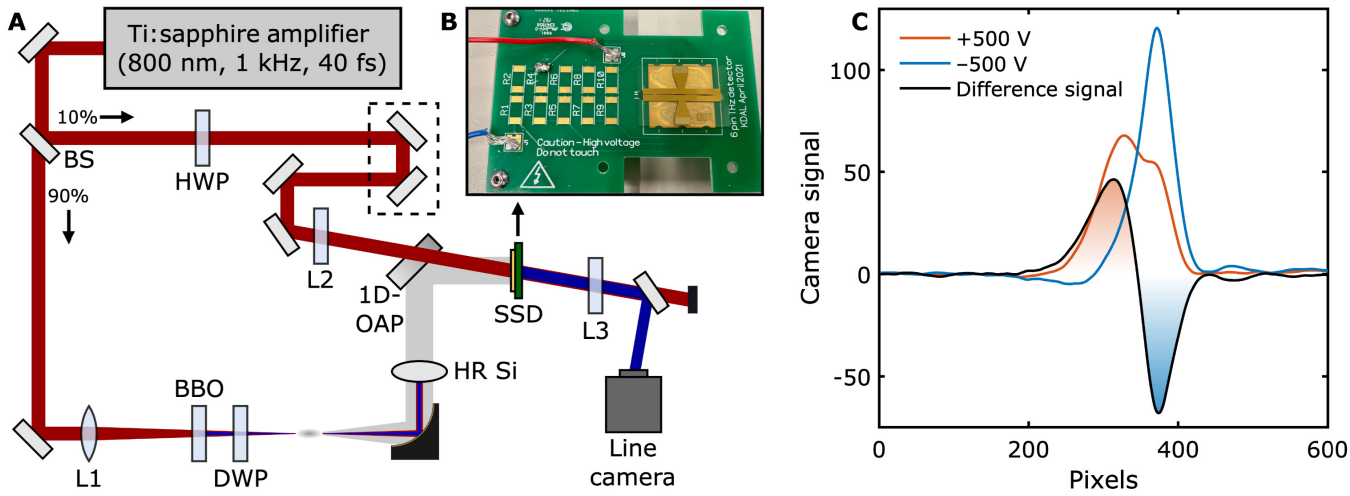

Fig. 2. (A) Top-view schematic of the experimental setup. L1: Plano-convex lens ($f = 300$ mm) for filament generation in air. BBO: Beta barium borate crystal (type I, thin) for 400-nm generation. DWP: Dual-wavelength waveplate (thin), $\lambda / 2$ for 800 nm and λ for 400 nm, yielding vertically polarized 800-nm and 400-nm beams. HWP: Half-wavelength waveplate for 800 nm, rotating the optical probe polarization to vertical. The dashed black rectangle marks the optical probe delay line. L2: Plano-convex cylindrical lens ($f =$ 150 mm) for focusing the optical probe to a line overlapping with the THz in the SSD. L3: Plano-convex cylindrical lens ($f = 100$ mm) for imaging the TFISH generated in the SSD onto the CCD line camera. (B) Image of the SSD. (C) Example of signals measured by the line camera after subtracting a constant, THz-independent background. The orange graph is measured with a 500-V bias applied across the active region of the SSD, and the blue graph is with the reverse bias voltage polarity applied. The black graph is the difference between the 2 signals, yielding a coherent measurement.

device optimization [20]. While most measurements including the results in Figs. 2C and 3 are conducted with a ±500-V bias, the results in Fig. 4 and Fig. S4 are obtained with a ±700-V detector bias. For standard ABCD systems with a point THz focus, the maximal air bias field (≈30 kV/cm) can effectively modulate and measure THz fields with peak strengths ranging from sub-kV/cm up to approximately 800 kV/cm, offering a good dynamic range ($> 10^3$, >60-dB power dynamic range) for THz waveform acquisition. However, modulation becomes insufficient for effective waveform detection when the THz field approaches or exceeds 1 MV/cm, requiring appropriate attention to the incident THz wave. Because of their significantly higher dielectric breakdown strength, SSD devices are capable of effectively modulating and, therefore, detecting THz waveforms with field strength up to the multi-MV/cm regime [20].

After filtering out the direct 800-nm beam with a combination of dichroic mirrors and bandpass filters centered around 400 nm, the generated TFISH line in the SSD is picked up by a charge-coupled device (CCD) line camera (Alphalas CCD-S3600-D-UV), which has a total of 3,648 pixels, each 8 μm wide and 200 μm tall (covering a total area of $29 \times 0.2\text{mm}^2$).

Obtaining coherent waveform detection

In the ABCD/SSBCD schemes, coherent waveform extraction is facilitated by applying a bias voltage across the detection region, yielding a bias field parallel to the probe and THz fields (here vertically polarized). The bias acts as a local oscillator, beating with the THz field and introducing a cross-term in the detected second harmonic signal, proportional to the electric field of the THz pulse. Obtaining a coherent waveform measurement involves extracting this cross-term. If the bias electric field applied across the detection region is much stronger than the THz electric field, the measurement will inherently be coherent, a scheme coined homodyne detection by Tomasino et al. [24]. The authors further showed that this requirement can be circumvented by repeating the homodyne detection measurement with the opposite bias voltage polarity applied and computing the difference between the 2 results, referred to as differential homodyne detection.

In traditional ABCD systems, it is common to alternate the bias voltage polarity between each laser shot and then directly compute the difference between the measured signal from 2 consecutive laser shots, known as heterodyne detection [25]. This scheme uses a signal generator to produce a high-voltage square wave oscillating at half the laser repetition rate. Since our camera has a limited frame rate (maximum 269.5 frames/second), we implement a quasi-heterodyne detection method. Here, the bias voltage is reversed after every 10 consecutive laser shots, while the camera integrates the total signal from these 10 shots. After 20 shots, a differential camera sensor signal is computed. The procedure can be repeated, and the measurement averaged for an increased SNR. Figure 2C shows an example of the resulting signals obtained with the camera through the quasi-heterodyne scheme (after averaging 1,000 times). The orange graph is the averaged signal with a 500-V bias applied, and the blue signal is with the reverse bias applied. They are both partially coherent. The difference between these, shown with the black graph, yields the purely coherent cross-term. While the differential homodyne scheme is simpler since it does not require a signal generator, it is highly dependent on the stability of the laser as well as the long-term stability of the DC high-voltage source and the SSD. In the quasi-heterodyne scheme, the square wave must exhibit minimal fluctuations. However, this approach is less sensitive to random noise on the detector, such as changes in ambient lighting.

Results and Discussion

System characterization

The spatial nonuniformity of the probe (Gaussian profile) and the THz line focus (collapsed donut-shaped profile; Fig. S2B)

causes the signal on the camera sensor to be nonuniform. This necessitates a calibration procedure. The calibration compensates for spatial variations and quantifies the time-to-space encoding of the optical setup, yielding a pixel-to-time conversion factor. It should be performed after completing or modifying the setup. Calibration involves coherent measurements at various translation stage positions, each corresponding to a specific probe-THz delay. The range of positions is chosen to ensure that each pixel records a complete waveform, including plateaus before and after. Figure S3 shows an example calibration scan with further details. After calibration, the signal across the camera sensor is uniform in magnitude, as seen in Fig. 3A. The slope of the dashed black line in this figure gives the probe-THz angle θ, enabling pixel-to-time conversion. In this case, $\theta = 1.4°$ over a 4.8-mm (600 pixels × 8 μm) wide detected signal, yielding a time window of approximately 400 fs and a temporal step size of 0.67 fs/pixel. This configuration corresponds to the data point on the line labeled with a TFISH width of 4.8 mm in Fig. 1B. All other data points in that figure were obtained similarly under different alignments.

Rasmussen et al. [23] recently quantified how the spectral content varies across the beam profile of 2-color air-plasma-based THz sources. Therefore, as the time-to-space encoding scheme presented here involves probing different positions in the THz beam profile, we expect a certain degree of spectral nonuniformity. Figure 3B depicts the THz power spectrum corresponding to the waveforms measured by each pixel in Fig. 3A. The calibrated system reveals slight spectral nonuniformity, particularly at the edges of the image. Since the nonuniformity is fully characterized through the calibration measurements, it should in principle be possible to compensate for it in post-processing. In the "THz-TDS of GaAs using the scanning-free scheme" section, we demonstrate that even with the observed spectral nonuniformity, we can still use the setup for spectroscopy and get excellent agreement with well-known material properties.

The blue graph in Fig. 3C is a horizontal cutout from Fig. 3A, marked with a blue dashed line, representing a camera-captured coherent waveform measurement where the pixels have been converted to probe-THz delay according to the obtained conversion factor. The orange graph in the same plot is a vertical cutout

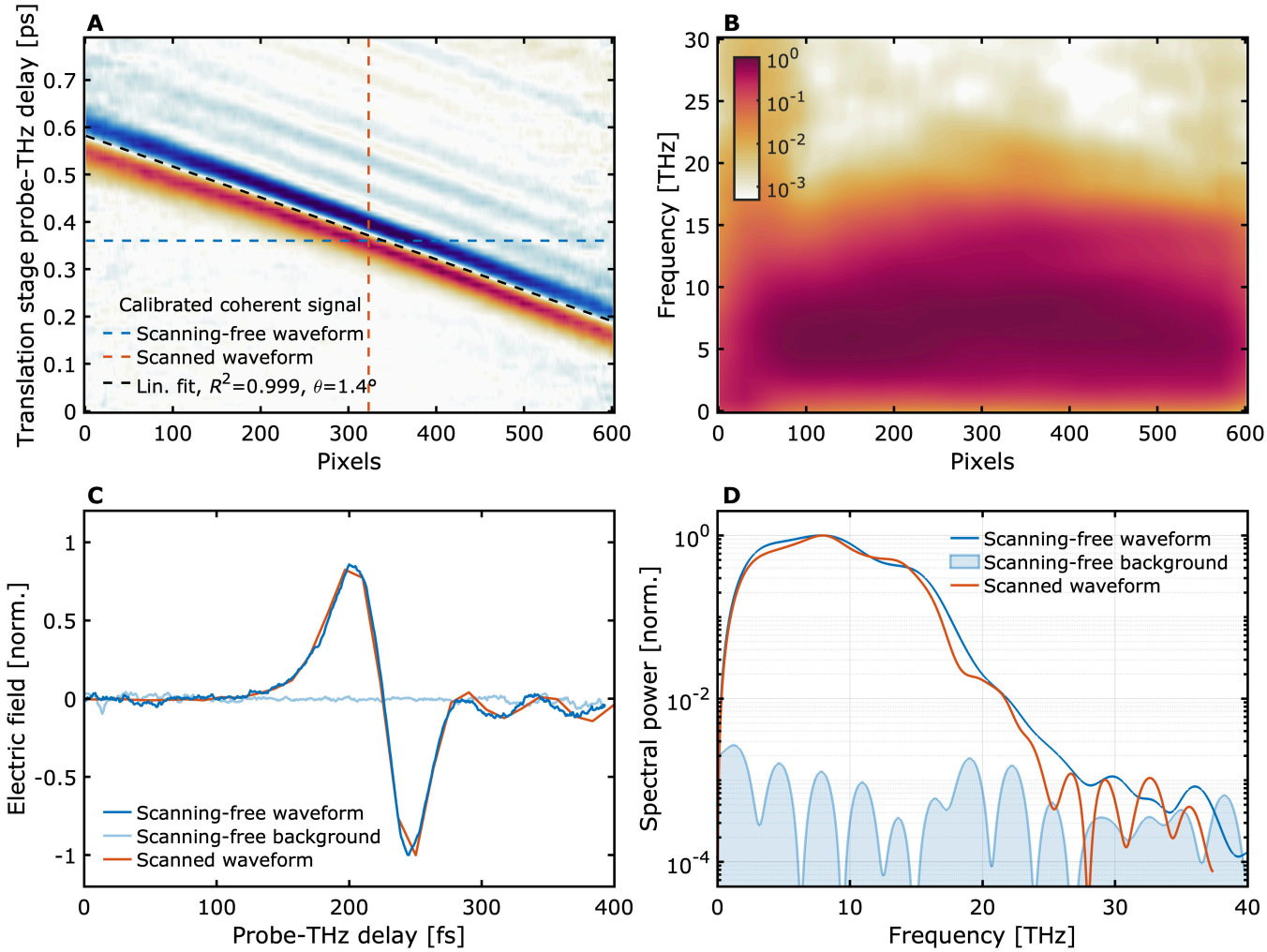

Fig. 3. (A) Waveforms captured with each pixel on the camera after calibration. Figure S3C is an uncalibrated version of this figure. The dashed black line is a linear fit to the THz waveform zero-crossing at every pixel and corresponding translation stage probe-THz delay. A probe-THz angle of 1.4° is obtained from the fit. The dashed blue line is a camera-captured waveform at a fixed translation stage probe-THz delay. The orange dashed line represents a waveform measured by a single pixel for different translation stage probe-THz delays. (B) Power spectral density (log scale, normalized) versus translation stage-defined frequency plotted for every pixel. (C) The blue graph corresponds to the dashed blue line in (A), and the light blue graph is the background measured in the absence of a THz signal. The orange graph similarly corresponds to the dashed orange line in (A). (D) Power spectrum of the signals in (C).

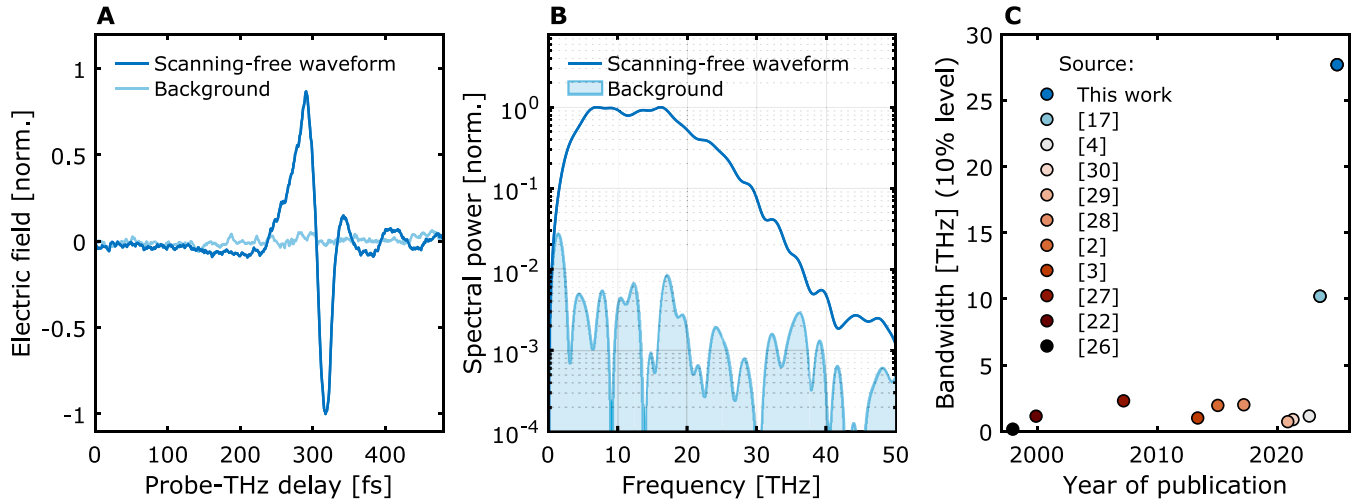

Fig. 4. (A) THz waveform (blue graph) and background signal (light blue graph) acquired with the scanning-free system with a 10-ms camera integration time and averaged over 1,000 times. Quasi-heterodyne detection is employed with a ±700-V detector bias voltage, meaning the total acquisition time is 2 × 10 s. (B) Intensity spectral density of signals in (A). (C) Maximal bandwidth of scanning-free THz waveform detection systems versus the year of publication. The bandwidth is defined as the frequency range extending 10 dB below the peak in the power spectral density of THz waveforms presented in the listed publications.

from Fig. 3A, representing a scanned waveform measured by a single pixel, emulating a point detector in a traditional SSBCD setup. The waveforms are highly similar and possess the same ultra-broad spectral bandwidth (see Fig. 3D). The camera-captured waveform is acquired in 20 s by averaging 20,000 laser shots, achieving a dynamic range of approximately 30 dB across an ultra-broad frequency range. However, in the following, we demonstrate that the bandwidth (see Fig. 4) and acquisition speed (see Fig. S4) can be further enhanced.

Ultra-broadband waveform acquisition

With careful optimization of the optical probe pulse duration onto the detection location and fine-tuning the overlap between the optical probe and THz line focuses, we achieve spectra with a bandwidth exceeding 30 THz. Figure 4A shows a camera-captured waveform with an associated bandwidth beyond 30 THz (Fig. 4B). For context, Fig. 4C summarizes the reported bandwidths of scanning-free THz coherent detection systems over the past 3 decades. Here, we define the bandwidth as the frequency range extending 10 dB below the peak power, as this is practically the most useful range for THz-TDS applications. Unlike other bandwidth definitions, which count from a certain dB level above the noise floor and typically increase with a higher spectral dynamic range due to longer measurement averaging, this definition is not influenced by the noise background level and spectral dynamic range, provided the dynamic range exceeds 10 dB. With this bandwidth definition, most of the systems have a maximum bandwidth of 2 THz [2–4,22,26–30]. A significant breakthrough utilizing TFISH generation within the same air plasma for THz emission extended the bandwidth to 10 THz on a single-shot basis, as indicated by the light blue dot in Fig. 4C [17,18]. Our results have further extended the bandwidth up to 28 THz (−10 dB) with spectrum components well exceeding 30 THz, limited only by the 40-fs optical probe pulse duration. Besides covering the entire THz region, the detection configuration is also completely compatible with THz-TDS since the detection process is isolated from the THz source itself, whether it is based on air plasma, solid-state, or liquid targets.

While the presented system is optimized for maximum detectable bandwidth on a scanning-free basis, many of the previous works shown in Fig. 4C focused on acquisition speed [4,29], or obtaining true one-shot waveform detection [2,17]. We have tested the minimum signal acquisition time necessary to record waveforms, and we can distinguish a waveform from the noise by integrating over 20 pulses (10 per bias voltage polarity), resulting in a total acquisition time of 20 ms (the spectral bandwidth is reduced due to the low SNR in this case). With a 10× longer acquisition time, 200 ms, the noise is significantly suppressed. In this setting, 5 waveforms can be recorded per second, enabling live waveform acquisition that supports the ultra-broadband nature of THz waveforms from 2-color air-plasma THz sources. These results are shown in Fig. S4.

In the following section, we demonstrate the application of the scanning-free system for ultra-broadband THz spectroscopy.

THz-TDS of GaAs using the scanning-free scheme

By inserting a 0.64-mm-thick gallium arsenide (GaAs) wafer in the THz beam path, the transmitted THz pulse is significantly attenuated and dispersed, as shown in Fig. 5A. The orange graph represents the THz wave after propagation through the GaAs sample, obtained by stitching together 5 consecutive camera measurements at different translation stage positions, thereby mapping out the dispersed waveform. This process of creating a longer time axis from individual camera-captured measurements can be automated. Notably, a similar approach has been effectively demonstrated by Nelson and colleagues [21] using their well-established high-speed echelon-based 2-dimensional THz spectroscopy platform.

The dispersed orange waveform exhibits high-frequency oscillations followed by lower-frequency oscillations, characteristic of GaAs. The corresponding spectrum in Fig. 5B and the absolute transmittance spectrum in Fig. 5C reveal that the transverse optical (TO) phonon in GaAs around 8 THz completely absorbs the frequencies within ±3 THz of the phonon. The absence of a transmitted signal in this range makes it impossible to compute a meaningful absorption spectrum. For this purpose, a reflection mode measurement would be more suitable. However, the blue

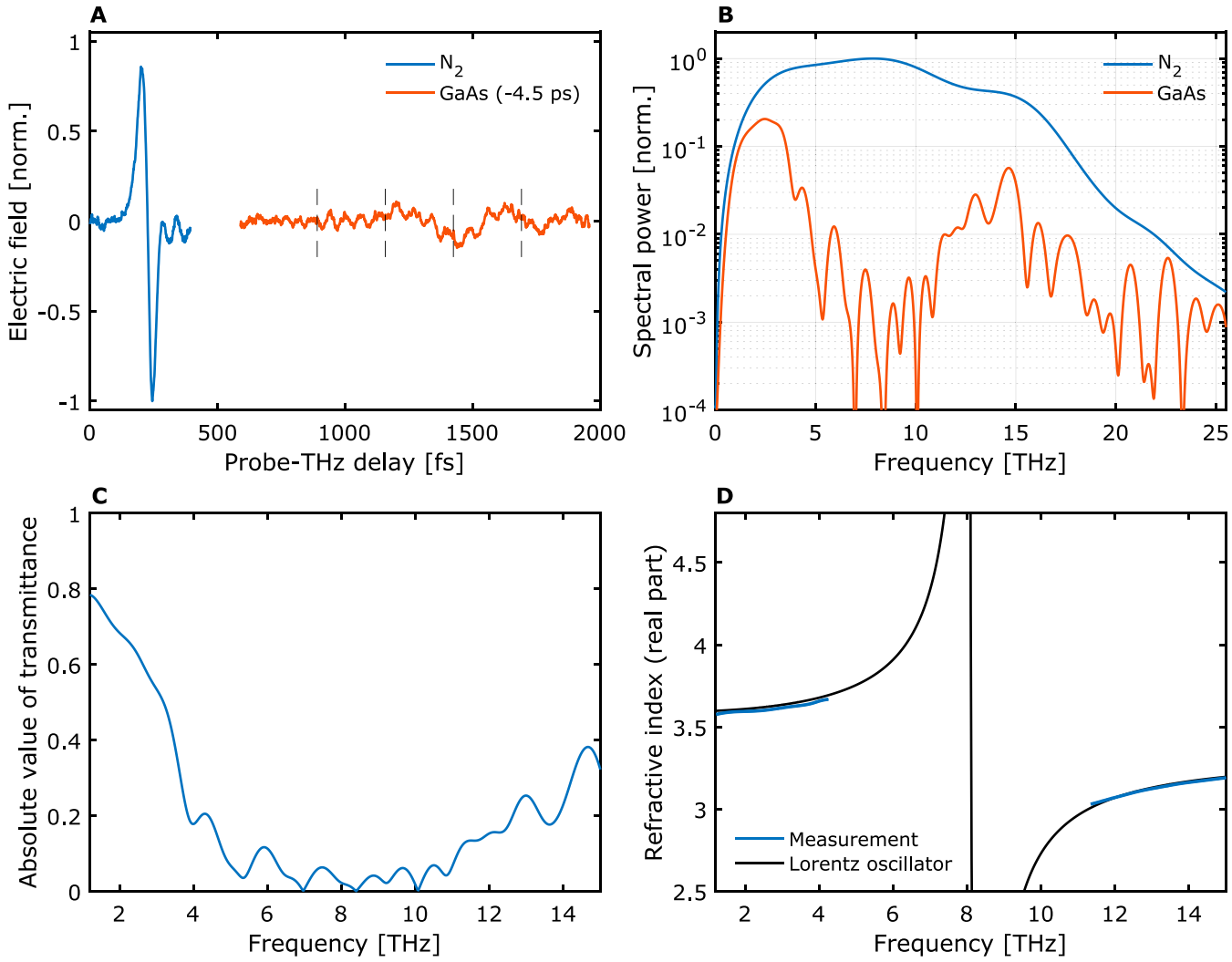

Fig. 5. (A) Blue graph: Reference THz waveform after propagation in N_2. It is the same waveform as in Fig. 3C. Orange graph: Sample THz waveform after propagation through a 0.64-mm-thick GaAs wafer and N_2, shifted 4.5 ps closer to the reference waveform for improved visibility. Obtained by recording and stitching together 5 waveforms with the same settings as the blue graph, but at different translation stage positions. (B) Intensity spectral density of signals in (A). (C) Absolute value of complex transmittance spectrum. (D) Blue graph: Refractive index spectrum of GaAs, extracted from measurements according to [31]. Black graph: Real part of refractive index, $n(\omega) = \sqrt{\epsilon(\omega)}$, as a function of frequency, $\omega / (2\pi)$, from Lorentz oscillator model of GaAs TO phonon. The complex permittivity model is $\epsilon(\omega) = \epsilon_\infty + A / (\omega_0^2 - \omega^2 - i\omega\Gamma)$ with parameters: $\epsilon_\infty = 10.99$, $A = 4{,}897\,\mathrm{ps}^{-2}$, $\omega_0 = 50.61\,\mathrm{ps}^{-1}$, $\Gamma = 0.471\,\mathrm{ps}^{-1}$ from [20].

graph in Fig. 5D shows the measured refractive index obtained through careful phase unwrapping and comparing it to a Lorentz oscillator model of the 8-THz TO phonon (black graph) [20,31]. The strong agreement demonstrates that the ultra-broadband scanning-free detection technique is fully compatible with THz-TDS applications.

Future improvements and paths toward single-shot operation

While the ultra-broadband, scanning-free detection technique has been successfully demonstrated, the current system requires extensive averaging to achieve waveforms with a high SNR. This limitation stems primarily from low TFISH generation along the detection line and the relatively low sensitivity of the specific line CCD camera. These issues result in weak and noisy readouts that significantly reduce the detection sensitivity and necessitate additional averaging.

In contrast, standard ABCD/SSBCD methods employ a point THz focus to generate the TFISH signal, which is then detected by highly sensitive devices such as photomultiplier tubes (PMTs) or avalanche photodiodes (APDs). These systems produce a single summed readout with superior sensitivity. However, the scanning-free detection scheme presents a unique challenge: The THz beam generating the TFISH is focused only in one dimension (line focus), resulting in at least 10 times lower field strength than the point-focus approach. Furthermore, the parallel detection setup requires sufficient signal readout across multiple pixels along the multimillimeter detection line, compounding the issue of limited TFISH generation. In this work, the THz line focus on the SSD achieves field strengths of several tens of kV/cm, calculated by following the methodology described in [32]. Scaling the field strength further using a 2-color air-plasma-based THz source driven by a 1-kHz Ti:sapphire laser amplifier remains challenging.

Conversely, high-energy THz pulses generated by larger-scale laser facilities offer a different scenario: Field strengths of 100 kV/cm or even MV/cm can be readily achieved along the THz line focus [5–7]. Such significantly stronger THz fields would result in an orders-of-magnitude enhancement of the TFISH line signal, dramatically improving detection sensitivity and waveform acquisition speed. Moreover, the applicable bias electrical field on the SSD is well-suited to modulate and detect these high THz field strengths, as discussed in the "Implementation" section. This highlights why the proposed system is particularly advantageous for detecting high-energy THz pulses produced by large-scale laser facilities.

In addition to strengthening the TFISH signal, adopting a faster and more sensitive camera for capturing TFISH line signals is critical for future improvement. While our current CCD line camera is functional, it is too slow for the 1-kHz THz signal repetition rate and has significantly lower sensitivity than PMTs or APDs. High-speed cameras with 10× better SNR and sensitivity, such as the JAI SW-4000M-PMCL or Princeton Instruments PIXIS-1024, are commercially available and could substantially enhance the scanning-free detection system with improved scanning speed and dynamic range of the acquired waveforms. Employing a high-speed camera is particularly important for achieving single-shot detection of THz sources operating at 1-kHz or higher repetition rate. Further optimization of the SSD device itself could also contribute to improved performance. A slightly thicker SiN film could enhance TFISH efficiency, provided the deposition process can maintain high quality at micrometer-scale thickness (see [20] for details on SiN film thickness considerations). Additionally, using thin films fabricated from materials with even higher $\chi^{(3)}$ could further boost TFISH efficiency, thereby improving the overall detection scheme.

By incorporating some of the abovementioned improvements, we anticipate significant gains in detection sensitivity while minimizing the need for data averaging. Although conventional biased detection schemes inherently require at least 2 shots for coherent waveform detection, a true single-shot waveform detection system can be realized by integrating a compatible balanced biased detection scheme into this scanning-free system [33].

Conclusion

By combining a novel high-sensitivity thin-film SSBCD technique with a noncollinear probe-THz geometry, we have demonstrated a scanning-free THz waveform detection system. This system can detect THz transients with a bandwidth exceeding 30 THz and is compatible with THz-TDS applications. The high detection sensitivity from the 1-μm-thin SiN active detecting media is crucial for this non-EO sampling-based technique, ensuring an intrinsic ultra-broad detection bandwidth and extremely fine time resolution. This detection configuration also provides the advantages of easily tunable temporal step size and total time window, making it more versatile than echelon-based configurations.

Given the simplicity of this scanning-free technique, it is particularly well-suited for high-energy THz pulses driven by large-scale laser facilities. With further advancements, we believe that the developed technique could not only provide key insights into intricate high-energy THz emission mechanisms in the relativistic regime but also, even more importantly, enable an ultra-high energy ultra-broadband THz-TDS platform for exploring extreme nonlinear material responses across the entire THz regime.

Acknowledgments

Funding: This work was supported by the Independent Research Fund Denmark (project THz-GRIP:2035-00365B).
Author contributions: A.H.O. and B.Z. conceived the concept for the work. A.H.O., B.Z., L.C., and P.U.J. designed the system. A.H.O. constructed the optical system with help from B.Z., P.U.J., and M.R. S.Z. designed and fabricated the solid-state detector with help from Y.D. A.H.O., L.C., and M.R. conducted the experiments and analyzed the data. A.H.O., B.Z., and P.U.J. prepared the manuscript. All authors contributed to finalizing and approving the manuscript.
Competing interests: The authors declare that they have no competing interests.

Data Availability

Data underlying the results presented in this paper are not publicly available at this time but may be obtained from the authors upon reasonable request.

Supplementary Materials

Supplementary Text
Figs. S1 to S4

References

1. Leitenstorfer A, Moskalenko A, Kampfrath T, Kono J, Castro-Camus E, Peng K, Qureshi N, Turchinovich D, Tanaka K, Markelz AG, et al. The 2023 terahertz science and technology roadmap. *J Phys D Appl Phys*. 2023;56:223001.
2. Teo SM, Ofori-Okai BK, Werley CA, Nelson KA. Invited article: Single-shot THz detection techniques optimized for multidimensional THz spectroscopy. *Rev Sci Instrum*. 2015;86(5):Article 051301.
3. Minami Y, Hayashi Y, Takeda J, Katayama I. Single-shot measurement of a terahertz electric-field waveform using a reflective echelon mirror. *Appl Phys Lett*. 2013;103:Article 051103.
4. Couture N, Cui W, Lippl M, Ostic R, Fandio DJJ, Yalavarthi EK, Vishhnuradhan A, Gamouras A, Joly NY, Menard J-M. Single-pulse terahertz spectroscopy monitoring sub-millisecond time dynamics at a rate of 50 kHz. *Nat Commun*. 2023;14(1):2595.
5. Pak T, Rezaei-Pandari M, Kim SB, Lee G, Wi DH, Hojbota CI, Mirzaie M, Kim H, Sung JH, Lee SK, et al. Multi-millijoule terahertz emission from laser Wakefield-accelerated electrons. *Light Sci Appl*. 2023;12(37):37.
6. Liao GQ, Li YT, Zhang YH, Liu H, Ge X-L, Yang S, Wei W-Q, Yuan X-H, Deng Y-Q. Demonstration of coherent terahertz transition radiation from relativistic laser-solid interactions. *Phys Rev Lett*. 2016;116(20):Article 205003.
7. Liao GQ, Liu H, Scott GG, Zhang Y-H, Zhu B-J, Zhang Z, Li Y-T, Armstong C, Zemaityte E. Towards terawatt-scale spectrally tunable terahertz pulses via relativistic laser-foil interactions. *Phys Rev X*. 2020;10:031062.
8. Sun FZ, Liao GQ, Lei HY, Wang T-Z, Wei Y-Y, Wang D, Chen H, Liu F, Li Y-T, Zhang J. A non-collinear autocorrelator

for single-shot characterization of ultrabroadband terahertz pulses. *Rev Sci Instrum*. 2022;93(12):Article 123003.
9. Jang D, Jin H, Kim KY. Single-shot terahertz spectrometer using a microbolometer camera. *Appl Phys Lett*. 2020;117:Article 091105.
10. Leitenstorfer A, Hunsche S, Shah J, Nuss MC, Knox WH. Femtosecond charge transport in polar semiconductors. *Phys Rev Lett*. 1999;82:5140–5143.
11. Park SB, Kim K, Cho W, Hwang SI, Ivanov I, Nam CH, Kim KT. Direct sampling of a light wave in air. *Optica*. 2018;5(4):402–408.
12. Liu Y, Beetar J, Nesper J, Gholam Mirzaei S, Chini M. Single-shot measurement of few cycle optical waveforms on a chip. *Nat Photonics*. 2022;16:109–112.
13. Ritzkowsky F, Yeung M, Bebeti E, Gebert T, Matsuyama T, Budden M, Mainz R, Cankaya H, Berggren K, Rossi G, et al. Large area optical frequency detectors for single shot phase readout. arXiv. 2023. https://doi.org/10.48550/arXiv.2306.01621.
14. Nomura Y, Wang YT, Kozai T, Shirai H, Yabushita A, Luo C-W, Nakanishi S, Fuji T. Single-shot detection of mid-infrared spectra by chirped pulse upconversion with four-wave difference frequency generation in gases. *Opt Express*. 2013;21(15):18249–18254.
15. Zhao Y, Kusama S, Furutani Y, Huang WH, Luo CW, Fuji T. High-speed scanless entire bandwidth mid-infrared chemical imaging. *Nat Commun*. 2023;14(1):3929.
16. Nomura Y, Shirai H, Fuji T. Frequency-resolved optical gating capable of carrier-envelope phase determination. *Nat Commun*. 2013;4:2820.
17. Garriga KJ, Francis XCZ. Local measurement of terahertz field-induced second harmonic generation in plasma filaments. *Front Optoelectron*. 2023;16(1):44.
18. Chong MLP, Francis KJG, Yiwen E, Zhang XC. Single-shot local measurement of terahertz correlated second harmonic generation in laser air plasma filaments. *Opt Lett*. 2024;49(2):226–229.
19. Tomasino A, Mazhorova A, Clerici M, Peccianti M, Ho S-P, Jestin Y, Pasquazi A, Markov A, Jin X, Piccoli R, et al. Solid-state-biased coherent detection of ultra broadband terahertz pulses. *Optica*. 2017;4(11):1358–1362.
20. Zhou B, Rasmussen M, Zibod S, Yan S, Noori NK, Nagy O, Ding Y, Lange SP, Dolgaleva K, Boyd RW, et al. Measurement of the dispersion of $\chi^{(3)}$ of SiO_2 and SiN across the THz and far-infrared frequency bands. *Laser Photonics Rev*. 2024;18(11):2301321.
21. Gao FY, Zhang Z, Liu ZJ, Nelson KA. High-speed two-dimensional terahertz spectroscopy with echelon-based shot-to-shot balanced detection. *Opt Lett*. 2022;47(14):3479–3482.
22. Shan J, Weling A, Knoesel E, Bartels L, Bonn M, Nahata A, Reider GA, Heinz TF. Single-shot measurement of terahertz electromagnetic pulses by use of electro-optic sampling. *Opt Lett*. 2000;25(6):426–428.
23. Rasmussen M, Nagy O, Skupin S, Stathopulos A, Berge L, Jepsen PU, Zhou B. Frequency-resolved characterization of broadband two-color air-plasma terahertz beam profiles. *Opt Express*. 2023;31(6):9287–9298.
24. Tomasino A, Piccoli R, Jestin Y, Drogoff BL, Chaker M, Yurtsever A, Busacca A, Razzari L, Morandotti R. Homodyne solid-state biased coherent detection of ultra-broadband terahertz pulses with static electric fields. *Nano*. 2021;11(2):283.
25. Karpowicz N, Dai J, Lu X, Chen Y, Yamagauchi M, Zhao H, Zhang X-C, Zhang L, Zhang C, Price-Gallagher M, et al. Coherent heterodyne time-domain spectrometry covering the entire "terahertz gap". *Appl Phys Lett*. 2008;92:Article 011131.
26. Jiang Z, Zhang XC. Electro-optic measurement of THz field pulses with a chirped optical beam. *Appl Phys Lett*. 1998;72:1945–1947.
27. Kim KY, Yellampalle B, Taylor AJ, Rodriguez G, Glownia JH. Single-shot terahertz pulse characterization via two-dimensional electro-optic imaging with dual echelons. *Opt Lett*. 2007;32(14):1968–1970.
28. Russell BK, Ofori-Okai BK, Chen Z, Hoffmann MC, Tsui YY, Glenzer SH. Self-referenced single-shot THz detection. *Opt Express*. 2017;25(14):16140–16150.
29. Baek IH, Kim H, Bark H, Jang KH, Park S, Shin J, Kim YC, Kim M, Oang KY, Lee K, et al. Real-time ultrafast oscilloscope with a relativistic electron bunch train. *Nat Commun*. 2021;12:6851.
30. Roussel E, Szwaj C, Evain C, Steffen B, Gerth C, Jalali B, Bielawski S. Phase diversity electro-optic sampling: A new approach to single-shot terahertz waveform recording. *Light Sci Appl*. 2022;11(18):14.
31. Jepsen P. Phase retrieval in terahertz time-domain measurements: A "how to" tutorial. *J Infrared Millim Terahertz Waves*. 2019;40(4):395–411.
32. Iwaszczuk K, Andryieuski A, Lavrinenko A, Zhang XC, Jepsen PU. Terahertz field enhancement to the MV/cm regime in a tapered parallel plate waveguide. *Opt Express*. 2012;20(8):8344–8355.
33. Ohrt AH, Nagy O, Loscher R, Saraceno C, Zhou B, Jepsen P. Balanced air-biased detection of terahertz waveforms. *Opt Lett*. 2024;49(18):5220–5223.